Appendix A

RHESSI Data Analysis Procedures and Tools

Since *RHESSI* is a relatively new mission, there is currently no comprehensive guidelines published in the literature for necessary steps to take when analyzing *RHESSI* data of a selected flare. Unlike many other missions, *RHESSI* provides time-tagged count rate data and image reconstruction is performed on the ground by individual users. This offers the users more freedom in choosing his/her own parameters (e.g., time and energy bins), but requires a higher level of proficiency of the data analysis software. It is thus necessary to document steps and related caveats for analyzing *RHESSI* data.

Here we present a comprehensive account of *RHESSI* data analysis procedures used for previous chapters in this book. There are some overlaps among the following sections, which we choose to keep for completeness of each section. These procedures are refinements to the standard *RHESSI* image reconstruction (Hurford et al., 2002) and spectral fitting (Smith et al., 2002) techniques that are implemented in the Interactive Data Language (IDL) routines available in the SolarSoftWare (SSW; Freeland & Handy, 1998). Specific analysis routines are described by Schwartz et al. (2002), in various documents on the *RHESSI* Web site,[1] and in the author's personal library (available upon request). The procedures described here can be readily adopted for other *RHESSI* data analysis tasks.

A.1 Flow Chart for Statistical Study of Imaging Spectroscopy (Chapter 2)

We summarize here the steps taken for the statistical study of imaging spectroscopy of limb flares presented in Chapter 2, which includes the following four parts:

I. Initial Screening: In the very first step, we scan the online flare list and narrow down our search range gradually as follows.

1. We use the two criteria (as stated in Chapter 2), longitude $\geq 70^\circ$ and peak count rate $\geq 30\,\mathrm{s}^{-1}\,\mathrm{detector}^{-1}$ in the 12–25 keV channel, to perform the initial selection. We

[1] See http://hesperia.gsfc.nasa.gov/rhessidatacenter/.

also require the highest energy band showing flare counts to be greater than 12 keV, in order to allow a sufficiently wide energy range for spectrum fitting.

2. Next we check various plots available online at the *RHESSI* data center to obtain a general impression for each selected flare. The *Quicklook Browser*[2] offers *RHESSI* light curves, images, spectrograms, and monitor rates. The spectrogram (by S. Krucker) shows the history of photon spectrum and can help distinguish between counts produced by flare photons and by radiation-belt particles, the latter of which usually appear as a blob at high energies. When checking the images, one should pay attention to the flare location, source morphology, and the highest imageable energy band. Note that this browser only provides *quicklook images* (by J. McTiernan) of a single time interval in broad energy bands and may miss the HXR peak(s) and thus FP emissions. The energy-by-time image array of a flare at the HESSI Experimental Data Center (HEDC) at ETH Zurich,[3] if available, is particularly useful for detailed inspection of images at separate times and energies. By examining these quicklook data sets, we can narrow down our focus to a sample of flares that show well-defined source structures (e.g., with clear LT and FP sources).

II. Preliminary Checking: Now we are ready to download the real flight data and conduct some more customized checks for each flare in the sample.

1. We can plot light curves through the *RHESSI* GUI widget and check various flags, including attenuator states, decimation (can be corrected since 2003/09/12), spacecraft night (eclipse), and South Atlantic Anomaly (SAA).

2. Some important information not shown in GUI can be obtained through J. McTiernan's quicklook flags (by get_flist_flag.pro and get_flag.pro from the author's personal library): (*a*) particle events; (*b*) upper energy limit and weight of decimation; (*c*) SC Transmitter (when it is on, detector 8 becomes noisy and should not be used); (*d*) NMZ and SMZ flags (which are on when *RHESSI* is at high magnetic latitudes, where the background is higher and the rear segments are decimated — 3 out of 4 counts are discarded below 150 keV. For energies $\lesssim$ 200 keV, one should use front segments only in this case.)

3. One can also check the spin period, aspect solutions, and suspected roll solutions (using chk_spin_aspect.pro and pmtras_analysis.pro). In the early stage of the mission, images should be integrated over a integer number of the spacecraft rotation period, but now this requirement is not necessary as long as the integration time is sufficiently long (at least half a spin, G. Hurford, 2005, private communication). However, bad aspect or roll solutions would affect the accuracy of positioning of images, and thus flares with this defect should generally not be included in our sample.

4. Pileup effects (see §A.4 for details) can be checked with hsi_check_pileup.pro (originally written by S. Krucker, using D. Smith's preliminary pileup correction). If the fraction of piled-up photons exceeds the 10% level of the total photons in energy band where

[2]http://sprg.ssl.berkeley.edu/~tohban/browser, by A. Y. Shih.
[3]http://www.hedc.ethz.ch/www/quick_dp_search.html

imaging spectroscopy will be conducted, the flare should be removed from our sample, as pileup corrections for imaging are not yet available. The above steps 2–4 can all be done with pre_chk_batch.pro.

III. Imaging: For the flares remaining in the sample after passing all the above selections, one must first reconstruct images from which spectra of individual sources can then be extracted.

1. Preliminary images of wide time intervals, broad energy bins, large pixel sizes, and large field of views can be made with the Back-projection or CLEAN algorithm which is computationally fast. The purpose here is to obtain the flare morphology at different energies and its general evolution. This step can be skipped if such images are available online (*Quicklook Browser* or HEDC) as mentioned above.

2. By checking the resulting images, one can identify ranges in time, energy, and space in which there are well-define X-ray sources. Within these ranges, one may make more CLEAN images with finer time and energy bins. Another way to determine the upper limit of the energy range for imaging is to check the spatially integrated spectrum, and identify the energy where the spectrum turns flat toward higher energies (dominated by the background) or becomes noisy with large fluctuations.

3. Based on the above experience with the flare under study, the user now needs to determine the control parameters for the final images which will be used for imaging spectroscopy. There are no universal rules here, but the general considerations (particularly regarding photon statistics) of time and energy bins can be found in §2.2. We shall emphasize that the number of energy bins should be large enough for spectral fitting, especially in the 10–30 keV range, in which the conjunction between thermal and nonthermal components appears. For example, one may take 16-20 logarithmically spaced energy bins in the 10–100 kev range. Note that the selected image dimension (field of view) can be as small as possible to save computational time, but must be large enough to enclose *all* the sources (Hurford et al., 2002).

4. Now one is ready to use the above selected control parameters to make the final images. We used the PIXON algorithm because of its superior photometry, but we must tolerate its computational expense. An error map, based on χ^2 estimates, can be obtained afterwards for each image. In instances when PIXON is computationally non-affordable, we used the CLEAN algorithm and saved the component and residual maps, the latter of which can be used for error estimates (see §A.2).

IV. Imaging Spectroscopy: Once the images are reconstructed, we can proceed to obtain the spectra of individual sources.

1. We need to first identify individual LT and/or FP sources in the images. It is useful to superimpose *RHESSI* images on *TRACE* and *SOHO* EIT EUV images, *SOHO* MDI[4] magnetograms and/or white-light images, and *GOES* Soft X-ray Imager (SXI)

[4]Conjugate FPs are usually located in magnetic fields of opposite polarities. For limb flares, large inclination angles (from line-of-sight) of magnetic field lines make it not very reliable to determine polarities from MDI magnetograms alone. However, if one overplots magnetograms and white-light maps together, one can identify individual sunspots and better estimate the polarities.

images, which help to identify the loop structure. However, oftentimes, we find a complex morphology and it is thus difficult to determine the source types (LT or FP) from images alone. Then, we will need to obtain additional information from the spectrum of each source (see below).

2. Once individual sources are identified, we can draw a box (or a circle or polygon) around each source and integrate the photon flux enclosed. It is advised (Hurford et al., 2002) that one must integrate a *whole* source to obtain its spectrum, and a spectrum inferred from a portion of a spatially unresolved source is not meaningful due to *RHESSI*'s limited spatial resolution. The uncertainties (see §A.2) of the integrated flux should be calculated as well for each box.

3. Now that we have obtained the spectrum and its uncertainty of each source, one can fit a model (e.g., thermal plus power-law or double power-law) to the data using Spectral Executive (SPEX) package (replaced by its object version since 2004). Note that the energy range that seriously suffers from pileup effects (§A.4) should be excluded (Emslie et al., 2003) from spectral fitting.

4. From the spectral fitting result, together with morphological information obtained above (step 1), we can now determine the source types with more confidence, because a LT source usually has a softer spectrum and a stronger thermal component than the corresponding FP sources. This step marks the end of the imaging spectroscopic analysis of one flare in the sample.

A.2 Notes for Imaging Spectroscopy

1. Detector Selection: For spectroscopic images, the front segments of detectors 3, 4, 5, 6, and 8 were used as default. For broad band images (for inferring light curves of individual sources), detectors 3–8 were usually used. Detector 2 was deselected due to its threshold of $\sim$25 keV and poor energy resolution of $\sim$9 keV. Detector 7 was generally not included for spectroscopy either because of its threshold of 7 keV and resolution of $\sim$3 keV. We did not use detector 1 because its $2.3''$ spatial resolution is smaller than most of the smallest features in our sample. Detector 9, due to its large FWHM resolution ($3'$ pitch), should be excluded for flares (especially those on the solar disk) that are located too close to the spin axis, because it is required that, for imaging purposes, any X-ray source must be away from the spin axis at a distance at least twice the FWHM resolution of any detector used (G. Hurford, Aug. 07, 2003, private communication).

2. Background Estimate: Since *RHESSI* is non-shielded spacecraft, the background level in the data is high (Smith et al., 2002). Various components contribute to *RHESSI* image background, falling into two categories (Aschwanden et al., 2004): (1) Non-flare photon flux neither modulated by the grids nor by the spacecraft rotation, including cosmic diffuse X-ray background, secondary photons from cosmic ray interactions with Earth's atmosphere and the spacecraft, spacecraft radioactivity, and bremsstrahlung in the Earth's atmosphere and the spacecraft from electrons precipitating from the radiation belts, etc. These background components appear as an overall DC offset, to the extent that they remain uniform over the spin period, in the modulation pattern (Hurford et al., 2002) and in the reconstructed images. This background category constitutes on the order of 1% of the total flare photons (T. Metcalf, 2003, private communication). (2) Flare-related flux not modulated by the grids but modulated by the spacecraft spin, i.e., flare photons that *bypass* the grids by Compton scattering at the spacecraft or Earth albedo, and flare photons that *pass* the grids but originate from large sources which are larger than the FWHM resolution of the coarsest grid used, including photons coming from outside the imaging field-of-view (FOV) or albedo photons reflected in the solar atmosphere and spread in a large FOV (G. Hurford, 2003, private communication). These fluxes form another category in image background which exhibit spatial structures and constitute on the order of 15% of the total flare flux (Aschwanden et al., 2004). A background model included in the PIXON (T. Metcalf, 2003, private communication) and forward-fitting algorithms (Aschwanden et al. 2002) attempts to remove the background flux of Category 2 from images. The way such a model works is to fit a sinusoidal function with a period of one and one half spacecraft spin period, respectively, to the modulation pattern and subtract the resulting fits from the count rate data. This background model was used for our PIXON images. We also took one more step in order to subtract the DC background flux of Category 1. To do this, we simply selected a sufficiently large box to enclose all flare sources. We then defined the rest of the image (excluding the selected box) as the background region, from which we obtained an average pixel value. For a given source with N pixels, the background flux (in units of photons cm^{-2} s^{-1} keV^{-1}) can be estimated as

$$b = \frac{a^2 N}{w} \times \frac{1}{M} \sum_{i=1}^{M} p_i \ , \tag{A.1}$$

where p_i is the individual pixel values (photons cm^{-2} s^{-1} arcsec^{-2}) in the background region, M is the corresponding number of pixels, a^2 (arcsec^2) is the area of a pixel, and w (keV) is the width of the energy bin. This DC background was then subtracted from the source flux.

3. Error Estimate: Error estimate for *RHESSI* images is currently a research topic (as of May 2008). Our first attempt involves two different approaches for CLEAN and PIXON images.

(1) For CLEAN images, we use the RMS of the residual map, $\sigma_{\rm rms}$, as the uncertainty of each pixel value. If the pixels were all independent, the flux error or uncertainty (in units of photons cm^{-2} s^{-1} keV^{-1}) for a source with N pixels and energy bin width w would be

$$\sigma = \frac{a^2}{w} \sqrt{\sum_{i=1}^{N} \sigma_{\rm rms}^2} = \frac{a^2}{w} \sqrt{N} \sigma_{\rm rms} \ , \tag{A.2}$$

where a is the size (in units of arcsecs) of each square pixel. However, the pixels inside a resolution element are dependent (spatially unresolved). We assume each resolution element to be a square with a size of the equivalent FWHM (arcsecs) of the detector combination used (e.g., FWHM=9.8$''$ for detectors 3–8) and thus with a number of pixels of $N_0 = ({\rm FWHM}/a)^2$. We further assume that the pixels inside an element have the same error, and therefore the flux error for each resolution element is $\sigma_1 = \frac{a^2}{w} N_0 \sigma_{\rm rms}$ rather than $\frac{a^2}{w}\sqrt{N_0}\sigma_{\rm rms}$. Since separate resolution elements inside a source are independent (spatially resolved), the resulting error for the whole source is

$$\sigma_* = \sqrt{N_1}\sigma_1 = \frac{a^2}{w}\sqrt{N_0}\sqrt{N}\sigma_{\rm rms} = \sqrt{N_0}\sigma = \left(\frac{\rm FWHM}{a}\right)\frac{a^2}{w}\sqrt{N}\sigma_{\rm rms} \ , \tag{A.3}$$

where $N_1 = N/N_0$ is the number of resolution elements inside the source. The factor $\sqrt{N_0} = {\rm FWHM}/a$ corrects for oversampling of choosing pixels smaller than the resolution element.

(2) For PIXON images, we use the hsi_calc_image_error.pro routine (by T. Metcalf) in the SSW package to get an error map that contains the pixel by pixel error, σ_i, of an image. Given the reconstructed model image, these errors are intended to provide a measure of how well each pixel is constrained by the data. This IDL routine determines how large a change in the image is required to produce a one sigma variation (based on χ^2) in the fit. A revision of the routine was made in December 2003 by T. Metcalf to take into account oversampling when determining the pixel error σ_i. Like that for CLEAN images, the error of the spatially integrated flux of a source is

$$\sigma_* = \left(\frac{\rm FWHM}{a}\right)\frac{a^2}{w}\sqrt{\sum_{i=1}^{N}\sigma_i^2} \ . \tag{A.4}$$

The resulting errors from these estimates are usually on the order of 10% at low energies (say, ~10 keV) and larger at high energies, which are comparable to the values obtained by the currently default error estimate algorithm in the *RHESSI* spectral analysis software called Object Spectral Executive (OSPEX). That algorithm uses $\frac{1}{3}$ of the maximum brightness outside the source region, presumably mainly contributed by the residual map in case of a CLEAN image, multiplied by the number of pixels in the source of interest (without correcting for oversampling). Saint-Hilaire et al. (2008, see their Appendix B) recently suggested that such errors are overestimated, and recommended $\frac{1}{6}$ in place of the scaling factor $\frac{1}{3}$.

A.3 Spectral Analysis for the 2002-04-30 M1.4 Flare with a Double Coronal Source (Chapter 4)

We document in this section the specific procedures adopted in Chapter 4 to obtain the spatially integrated spectra throughout the 2002 April 30 M1.4 flare and the spatially resolved spectra of the two individual coronal sources during the first HXR peak.

A.3.1 Spatially Integrated Spectra

For the spatially integrated spectra we used the standard forward-fitting method implemented in the object-oriented routine called OSPEX and described in Brown et al. (2006). OSPEX uses an assumed parametric form of the photon spectrum and finds parameter values that provide the best fit in a χ^2 sense to the measured count-rate spectrum in each time interval.

In analyzing the *RHESSI* spatially integrated count-rate spectra we took advantage of the fact that *RHESSI* makes nine statistically independent measurements of the same incident photon spectrum with its nine nominally identical detectors. By analyzing the data from each detector separately, up to nine values can be obtained for each spectral parameter. The scatter of these values about the mean then gives a more realistic measure of the uncertainty than can be obtained from the best fit to the spectrum summed over all detectors. In addition, treating each detector separately allows us to use the $\frac{1}{3}$ keV wide "native" energy bins of the on-board pulse-height analyzers for each detector. This avoids the energy smearing inherent in averaging together counts from different detectors that have different energy bin edges and sensitivities. We limited the total number of energy bins by using the $\frac{1}{3}$ keV native bins only where they are needed, i.e., between 3 and 15 keV. This provides the best possible energy resolution that is important in measuring the iron and iron-nickel line features at $\sim$6.7 and $\sim$8 keV, respectively (Phillips, 2004), and the instrumental lines at $\sim$8 and $\sim$10 keV. We used 1 keV wide energy bins (three native bins wide) at energies between 15 and 100 keV, where the highest resolution was not needed to determine the parameters of the continuum emission in this range.

We recommend the following sequential steps, which we generally followed, to obtain the "best-fit" values of the spectral parameters and their uncertainties in each time interval throughout the flare.

1. Select a time interval that covers all of the *RHESSI* observations for the flare of interest. Also include times during the neighboring *RHESSI* nighttime just before and/or just after the flare for use in determining the nonsolar background spectrum.

2. Accumulate count-rate spectra corrected for livetime, decimation, and pulse pileup (Smith et al. 2002; although it is best to correct pileup in step 6 below) for each of the nine detectors in 4 s time bins (about one spacecraft spin period) for the full duration selected in step 1 above. A full response matrix, including off-diagonal elements, is generated for each detector to relate the photon flux to the measured count rates in each energy bin.

3. Import the count-rate spectrum and the corresponding response matrix for one of the detectors into the *RHESSI* spectral analysis routine, OSPEX. We used detector 4, since it has close to the best energy resolution of all the detectors.

4. Select time intervals to be used in estimating the background spectrum and its possible variation during the flare. In general, nighttime data must be used if the attenuator state changes during the flare; otherwise pre- and/or postflare spectra can be used. Account can be taken of orbital background variations during the flare by using a polynomial fit to the background time history in selectable energy ranges or by using the variations at energies above those influenced by the flare. For this event, since the thin attenuator was in place for the whole duration of the flare, a preflare interval was used for background estimation.

5. Select multiples of the 4 s time intervals used in step 2 that are long enough to provide sufficient counts and short enough to show the expected variations in the spectra as the flare progresses. Be sure that no time interval includes an attenuator change. For this event, we selected the seven time intervals marked in Figure 4.1 covering the first HXR peak.

6. Fit the spectrum for the interval near the peak of the event to the desired functional form. Spectra can be fitted to the algebraic sum of a variety of functional forms, ranging from simple isothermal and power-law functions to more sophisticated models, such as various multi-thermal models and thin- and thick-target models with a power-law electron spectrum having sharp low- and high-energy cutoffs. In our case, we assumed that an isothermal component plus a double power law provides acceptable fits to the measured count-rate spectra in most cases. This simple two-component model is sufficient to capture the key physics for this flare, i.e., to estimate the relative contributions of the thermal and nonthermal components of the X-ray emission.

   The isothermal spectrum was based on the predictions using the CHIANTI package (ver. 5.2, Dere et al., 1997; Young et al., 2003) in SSW with Mazzotta et al. (1998) ionization balance. The iron and nickel abundances were allowed to vary about their coronal values to give the best fit to the iron features in the spectra.

   For simplicity, we set the power-law index below the variable break energy to be fixed at $\gamma = 2$ to approximate a flat (constant) electron flux below a cutoff energy. The value of γ above the break energy and the break energy itself were both treated as free parameters in the fitting process.

   We also included several other functions to accommodate various instrumental effects. These included two narrow Gaussians near 8 and 10 keV, respectively, to account for two instrumental features that may be L-shell lines from the tungsten grids. The thin attenuator was in place during the entire course of the flare, thus restricting us from fitting the spectra below $\sim$6 keV.

   Another routine available in OSPEX was used to both offset the energy calibration and change the detector resolution to better fit the iron-line feature at $\sim$6.7 keV. This is important at high counting rates when the energy scale can change by up to $\sim$0.3 keV.

   Pulse pileup can best be corrected for at this stage by using a separate routine with count-rate–dependent parameters, although this is still in the developmental stage and was not used for this chapter. However, the average livetime (between data gaps) during the impulsive peak (interval 1, 08:20:27–08:20:56 UT) of this M1.4 flare was 93.4%. This is to be compared with the values of 55% and 94% for the 2002 July 23 X4.8 flare and the 2002 February 20 C7.5 flare, respectively. In addition, the estimated ratio of piled-up counts to the total counts is below 10% at all energies, indicating very minor pileup effects on the spectra of this event. A more detailed account on estimating pileup severity can be found in §A.4.1 (also Liu, W. et al., 2006, their §2.1) in general and in §A.4.2 (also Liu, W. et al., 2008a) for imaging spectroscopy in particularly.

It is important to use good starting values of the parameters to ensure that the minimization routine converges on the best-fit values. These were obtained for detector 4 in the interval at the peak of the flare by experienced trial and error.

7. Once an acceptable fit (reduced $\chi^2 \lesssim 2$, with the systematic uncertainties set to zero) is obtained to the spectrum for the peak interval, OSPEX has the capability to proceed either forwards or backwards in time to fit the count-rate spectra in other intervals using the best-fit parameters obtained for one interval as the starting parameters to fit the spectrum in the next interval. This reduces the time taken to fit each time interval, but various manual adjustments are usually required to the fitted energy range, the required functions, etc., in specific intervals to ensure adequate fits in each case with acceptable values of χ^2.

8. The best-fit parameters found for each time interval for the one detector chosen in step 3 are now used as the starting parameters in OSPEX for the other detectors. In this way, acceptable fits can be obtained in each time interval for all nine detectors. In practice, it is usually not possible to include detectors 2, 5, or 7 in this automatic procedure, since they have higher energy thresholds and/or poorer resolution compared to the other detectors.

9. The different best-fit values (in practice, only six were obtained) of each spectral parameter can now be combined to give a mean and standard deviation. These values then constitute the results of this spectral analysis and can be used for further interpretation as indicated in Chapter 4. For display purposes, it is important to show the best-fit photon spectrum computed using these mean parameters with some indication of the photon fluxes determined in each energy bin from the measured count rates. For this purpose, we have chosen to display the photon fluxes averaged over all detectors used in the analysis (all but detectors 2, 5, and 7). The photon flux of each detector was determined by taking the count rate and folding it through the corresponding response matrix with the assumed photon spectrum having the best-fit parameters. This gives a reasonable representation but it is well known that data points determined in this way are "obliging" and follow the assumed spectrum (Fenimore et al., 1983, 1988). Hence, such plots (Fig. 4.6) should be viewed with caution. Also note that the χ^2 values of the averaged photon fluxes are not necessarily representative of the independent fits to the data of individual detectors.

A.3.2 Spatially Resolved (Imaged) Spectra

In order to determine the photon spectra of the two distinct sources seen in the X-ray images, we used *RHESSI* 's imaging spectroscopy capability and carried out the following steps.

1. We selected the same seven intervals (marked in Fig. 4.1) as those used for the spatially integrated spectra.

2. For each selected time interval, images in narrow energy bins ranging from 1 keV wide at 6 keV to 11 keV wide at 50 keV were constructed using the computationally

expensive PIXON algorithm (Metcalf et al., 1996), which gives the best photometry and spatial resolution (Aschwanden et al., 2004) among the currently available imaging algorithms. Detectors 3, 4, 5, 6, and 8 covering angular scales between 6.8″ and 106″ were used to allow the two sources to be clearly resolved. No modulation was evident in the detector 1 and 2 count rates, showing that the sources had no structure finer than the 3.9″ FWHM resolution of detector 2.

3. The PIXON images were imported into OSPEX for extracting fluxes of individual sources. Note that the images are provided in units of photons $\mathrm{cm^{-2}\ s^{-1}\ keV^{-1}\ arcsec^{-2}}$, using only the *diagonal* elements of the detector response matrix to convert from the measured count rates to photon fluxes. OSPEX converts the images back to units of counts $\mathrm{cm^{-2}\ s^{-1}\ keV^{-1}\ arcsec^{-2}}$, using the same diagonal elements and then uses the *full* detector response matrix, including all off-diagonal elements, to compute the best-fit photon spectrum (photons $\mathrm{cm^{-2}\ s^{-1}\ keV^{-1}}$) for each source separately. The summed count rates in the two boxes shown in the middle panel of Figure 4.2 around the average positions of the two sources were accumulated separately for each image in each energy bin. The boxes were adjusted accordingly for each time interval if the sources moved. (Note that only a single box was used for interval 1 when only the lower source was detected.)

4. The uncertainties in the count rates were calculated from the PIXON error map based on χ^2 variations of the reconstructed image (see Appendix §A.2). The errors were originally obtained in photon space and then converted in the same way described above to count space where the actual fitting was performed.

5. The two independent count-rate spectra, one for each source, were then fitted independently to the same functions used for the spatially integrated spectra as described earlier. We further demand that the iron abundance of the thermal component and the break energy of the double power law be fixed at the values given by the fit to the corresponding spatially integrated spectrum in the same time interval. This makes the spectra directly comparable for our purposes. Note that the error bars of the imaging spectral parameters are obtained from the χ^2 variation during the fitting procedure. At times when such an error is smaller than that of the corresponding spatially integrated spectrum, the latter value is used instead.

Finally, for a self-consistency check, we have compared the sum of the imaging spectra of the two sources with the spatially integrated spectrum and found that they are consistent. The only exception is at the low energies ($\lesssim$10 keV) where the imaging spectra do not have enough resolution for us to see the iron-line feature.

A.4 Effects of Pulse Pileup

Pulse pileup refers to the phenomenon that two or more photons close in time are detected as one photon with their energies summed (Smith et al., 2002). When count rates are high, as happens in large flares, an artifact appears in the measured spectrum at twice or a larger multiple of the energy of the peak of the count rate spectrum that is at ~6 keV in the *RHESSI* attenuator A0 state, ∼10 keV in the A1 state, and ∼18 keV in the A3 state. Unfortunately, due to the nonlinear complexity of the problem, there is currently no 100% reliable pileup correction algorithm available in the *RHESSI* software, especially for imaging spectroscopy. For spatially integrated spectra, the only available correction algorithm is the preliminary one of Smith et al. (2002), while another one is under development by R. Schwartz as of May 2008; for imaging spectroscopy, there is no existing correction at all. Below we discuss pileup effects in greater detail for two individual flares addressed in the main body of this book.

A.4.1 Pileup Effects for the 2003-11-13 M1.7 Flare (Chapter 6)

It is necessary to check if pulse pileup is important in the 2003 November 13 M1.7 flare (Chapter 6) before we can make a more quantitative interpretation of the data. There are several ways to do the check, the first and simplest of which is the detector livetime, i.e., the complement of the deadtime during which the detector is not able to distinguish among different incident photons. We first accumulated spatially integrated spectra for every 1 s time bin during the interval of 04:58:01-04:59:49 UT,[5] using the front segments of all nine detectors except detectors 2 and 7, which have degraded energy resolution (Smith et al., 2002). We then obtained the fractional livetime (between data gaps) from the spectrum object data and averaged it over the seven detectors being used. The resulting livetime generally decreases with time, ranging from 96% to 89%, with a small modulation produced by the spacecraft spin. In this M1.7 flare, such a livetime is comparably high (cf. the livetime of $\sim 55\%$ during the 2002 July 23 X4.8 flare and of $\sim 94\%$ during the 2002 February 20 C7.5 flare) and indicates minor pileup severity.

Another approach involves inspecting the change of the spectrum due to pileup. We accumulated spectra over each spacecraft spin period (~ 4 s, with the same set of detectors mentioned above) and used the pileup correction to obtain the relative fraction of the pileup counts among the total counts as a function of energy (Smith et al., 2002). We find that the pileup counts amount to less than $\sim 10\%$ of the total counts at all energies until 04:59:01 UT, when the livetime drops to 91%. After that, the relative importance of the pileup counts continues to increase, but remains below $\sim 20\%$ of the total counts before 04:59:17 UT. Toward the end of the first HXR pulse (04:59:45-04:59:49 UT, livetime of $\sim 90\%$), the ratio of pileup counts to total counts exceeds 10% in the entire 20-40 keV range and humps up to 43% near 28 keV. We integrate both the pileup counts and total counts over the 20-40 keV band and plot their ratio versus time as a general indicator of pileup severity (see Fig. A.1). Clearly this ratio is $\lesssim 15\%$ during the first two-thirds of the interval shown and does not reach the moderate $\sim 25\%$ level until the very end.

We therefore conclude that pileup effects are generally not very significant for this flare, especially during the first minute of the impulsive phase, because the count rate is not too high and the thin shutter is in during the time interval of interest, which further attenuates the count rate. It should be noted that the two piled-up photons (that result in a single photon seen in the image) most probably originate from the same location on the Sun, and pileup of photons across different sources is relatively unimportant (G. Hurford, 2006,

[5] This time interval is also used in studying the evolution of the source morphology in §6.2.1 (see text about Fig. 6.5), which covers the bulk of the first HXR pulse.

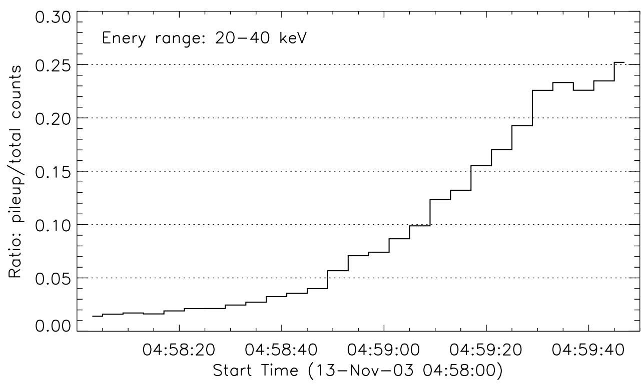

Figure A.1: Ratio of pileup counts to total counts, both integrated over the 20-40 keV range in time bins of one spacecraft spin for the 2003 November 13 M1.7 flare [from Liu, W. et al. 2006].

private communication). Therefore, the source geometry would not be significantly affected by pileup, except that there could be a "ghost" of a low-energy source appearing in a high-energy image for very large (e.g. X-class) flares (see, e.g., §A.4.2). However, the spectra of individual sources derived from images are distorted, which is relatively more significant at the LT than at the FPs. This is because low-energy photons dominate over high-energy photons in population, and have the highest probability to produce pileup, and generally most of the low-energy photons are emitted by the LT source.

A.4.2 Pileup Effects on Imaging Spectroscopy for the 2003-10-29 X10 Flare (Chapter 5)

It is necessary to assess the importance of pileup and its effects on our interpretation of *RHESSI* data for the 2003 October 29 X10 flare (Chapter 5). We have adopted and improved upon the several ways to estimate the pileup severity and minimize its effects described above (§A.4.1).

Figure A.2*a* shows the history of the fractional livetime (*thin line*), as a general indicator of pileup severity, averaged over detectors 3–9 and over 4 s intervals, which generally anti-correlates with the detector count rate. It decreases (from 96%) as the flare progresses toward its impulsive peak and reaches its minimum of 24% at 20:46:10 UT. This value is very small compared with the livetime minima of 55% during the 2002 July 23 X4.8 flare and 94% during the 2002 February 20 C7.5 flare, and thus indicates severe pileup effects. We can further check the detailed livetime variation on a 0.1 s cadence, as shown in Figure A.2*b* for detector 9. The modulation caused by the coarse grids (FWHM of 183″) above detector 9 during the spacecraft rotation with a ∼4 s period is clearly seen. That is, during each modulation period, the livetime cycles between its minimum and maximum values in anti-correlation with the count rate. The fractional livetime varies between about 5% and 70%. Knowing the way *RHESSI* makes images (Hurford et al., 2002), this fine temporal variation makes pileup correction for imaging spectroscopy even more difficult than for the spatially integrated spectra.

In addition to livetime, it is more informative to examine how pileup affects the shape of the spectrum. We thus performed pileup corrections to the spatially integrated spectra using the preliminary algorithm of Smith et al. (2002). Figures A.2*c* and A.2*d* show an example of the measured and pileup-corrected count-rate spectra, the first- and second-order pileup spectra, and the ratio of the piled-up to total counts. As is evident (Fig. A.2*d*), the fraction of the piled-up counts is negligibly small at low energies, which amounts to less than 1% (below 18 keV) and less than 10% (below 26 keV). The most obvious alteration of the spectrum shape occurs in the 30–40 keV range in which 36 keV is twice the energy (18 keV) of the peak in the count-rate spectrum (in the A3 attenuator state) and thus the peak of the first order (two photons counted as one) piled-up spectrum. In this energy range pileup produces a small artificial hump in the measured spectrum, which results from a corresponding reduction of counts at low energies (15–20 keV). Above 50 keV, although the

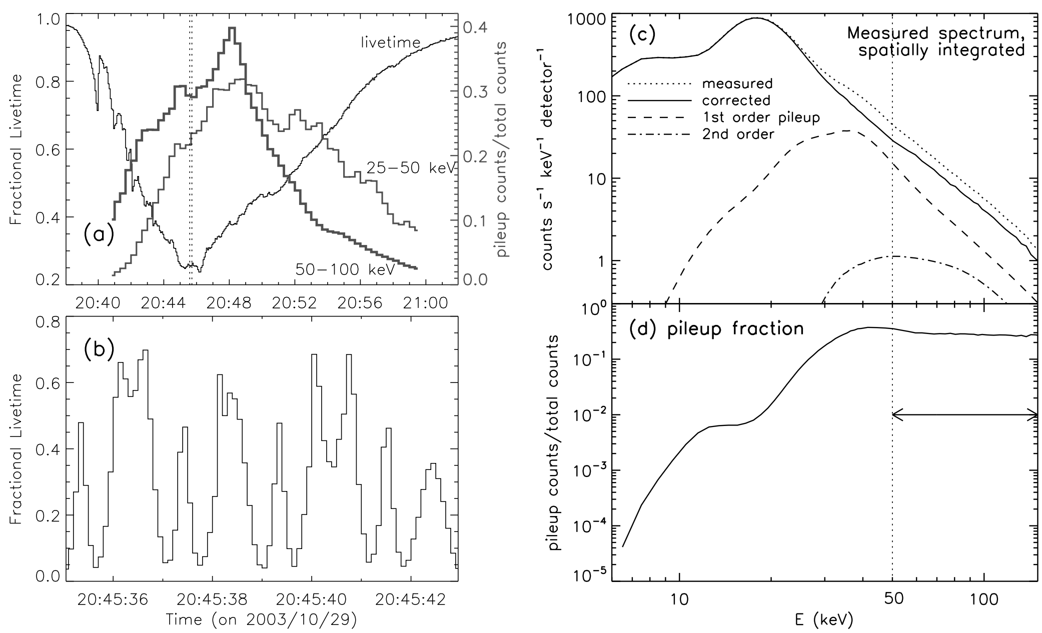

Figure A.2: Assessment of pileup severity for the 2003 October 29 X10 flare. (*a*) Fractional livetime (excluding data gaps, *thin line, left scale*) averaged among detectors 3–9 (used for the images presented in Chapter 5) over 4 s intervals as a function of time. Overlaid are the fractions of the counts recorded in the two energy bins of 25–50 and 50–100 keV that are piled up (*thick lines, right scale*), estimated with the algorithm of Smith et al. (2002). (*b*) Fractional livetime of detector 9 with a 0.1 s cadence during an 8 s interval marked by the two vertical dotted lines in (*a*). The modulation is caused by the changing count rate produced by the grids above the detector as the spacecraft rotates. (*c*) Count rate spectrum averaged over detectors 3–9 for interval 20:46:00–20:46:20 UT covering the livetime minimum in (*a*). The dotted and solid lines are the measured and pileup corrected spectra (Smith et al., 2002), respectively. The dashed and dot-dashed lines are the first- (two photons) and second-order (three photons) piled-up spectra estimated from the measured spectrum, with their peaks marked by the vertical dotted lines at 36 and 54 keV, respectively. (*d*) The fraction of the total recorded counts as a function of energy that are piled up (including first- and second-order pileup) [from Liu, W. et al. 2008a].

they are different in absolute values, the pileup corrected and measured spectra are almost parallel (Fig. A.2*c*), and the pileup fraction is almost constant with a relative variation

<30% (Fig. A.2*d*). We also integrated the piled-up counts and obtained their ratios to the total counts in the 25–50 and 50–100 keV bands, which are shown in Figure A.2*a* vs. time as a another general indicator of pileup importance.

In Chapter 5 we are specifically interested in the spatially resolved spectra of the LT and FP sources. Because of the rotational modulation nature of *RHESSI* image reconstruction (Hurford et al., 2002), pileup has quite different effects on imaging spectroscopy compared with effects on the spatially integrated spectrum discussed above. Such effects can be avoided or alleviated in various ways, which can make imaging spectroscopy less affected by pileup than spatially integrated spectroscopy (R. Schwartz, private communication). The specific effects are as follows: (1) As noted above (§A.4.1), pileup of photons from two or more spatially resolved sources is generally insignificant in images. This is more true for finer grids because two photons must come from the same region within the FWHM resolution of the grid in order to pileup as one photon in the underlying detector. We used uniform weighting (Hurford et al., 2002) for image reconstruction, which assigns higher weights for finer grids and thus de-emphasizes pileup of photons originating from within a large source area that is included in the FWHM of coarser grids. (2) Among all the sources, LT suffers the most from pileup compared to the FPs. This is because pileup depends on count rates. Most of the detected photons in the A3 state have energies below ∼20 keV where the LT source dominates, while the FPs dominate at higher energies where the photon flux is much lower. (3) As noted above, the peak of the count-rate spectrum of this flare (in the A3 attenuator state) is ∼18 keV. The majority of pileup results from photons around this energy and appears as a ghost LT source (e.g., Fig. 5.3*i*) at energies around 36 keV (see Fig. A.2*c*). Therefore, below ∼25 keV, pileup at the LT source is negligible; above ∼50 keV, the shape of the FP spectrum is most likely not affected by pileup, and only the flux is elevated by a constant factor independent of energy up to 150 keV because of second and higher order pileup due to high count rates in this flare. (4) In addition, we are mainly concerned with the similarities and differences of HXR fluxes and spectral shapes (power-law indexes) between the two FP sources, which may be even more insensitive to pileup. This is because the percentage of piled-up counts among the measured counts of the two FPs are likely to be very similar and thus the two FPs are affected to similar extents. In our imaging spectroscopic analysis, we have thus fitted the LT spectra only below 20 keV and the FP spectra only above 50 keV in order to minimize pileup effects. This 50 keV was also used by Emslie et al. (2003) and Saldanha et al. (2008) as the lower limit of the energy range for fitting the (FP) spectra of X-class flares in which pileup is important.

A.5 *RHESSI* Simulation Tool and Its Applications

One of the advantages of the *RHESSI* software is the inclusion of the simulation tool, developed and maintained by J. McTiernan. A user can specify a model source morphology together with a photon spectrum, and use this model as an input to the simulation software. Then the software will generate images based on a user-specified image reconstruction algorithm (Hurford et al., 2002), taking into account the real instrument response, as if they were seen through the "eyes" of *RHESSI*. This can help user better understand observed flare morphology and distinguish reality from artifacts.

We have frequently used this simulation tool in our *RHESSI* data analysis. One of the examples was to simulate the emission profile along a loop in which thermal conduction is or is not suppressed and compare the results with the observed profile. Details of this study can be found in Jiang et al. (2006).

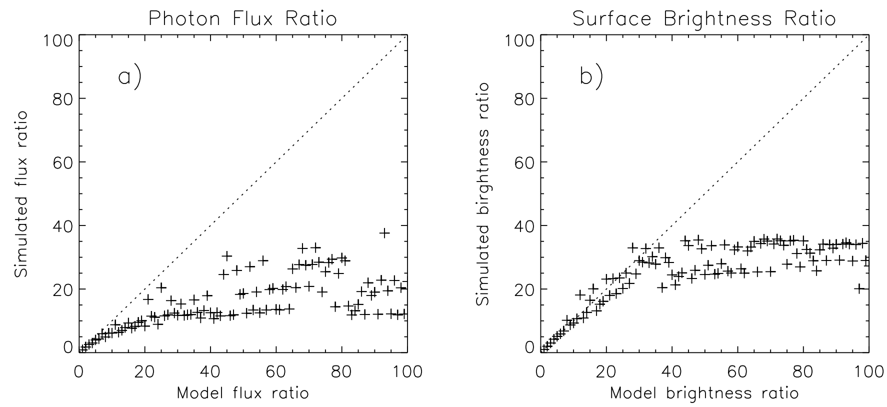

Figure A.3: (a) Simulated HXR photon flux ratio vs. input model flux ratio, obtained from the *RHESSI* simulation software. The dotted diagonal line indicates a perfect instrument response. (b) Same as (a) but for surface brightness.

Another example of simulation is testing the *RHESSI* dynamic range. Here we input an image with a size of $64'' \times 64''$ ($1''$ pixel), in which two $3'' \times 3''$ uniform sources were placed along the diagonal line, with their centers located at $x = 21''$ and $x = 46''$, respectively. We then fixed the surface brightness of one source at 1 unit (arbitrary scale) and varied that of the other from 1 to 100 units, for each of which we ran the simulation software with the CLEAN algorithm to obtain an output image. Afterwards we calculated the ratio of the spatially integrated flux as well as the maximum surface brightness of the two sources. The simulated ratios (as of August 2003) are plotted against the corresponding input (model) ratios in Figure A.3. As we can see, the surface brightness ratio can preserve the model input value up to about 30, beyond which the simulated ratio becomes flat. This simulation suggests a dynamic range of $\sim$30 for surface brightness, higher than the nominal value of 10 as of 2003. The dynamic range for the integrated flux is slightly less than 10, because there are photons registered beyond the finite integration area in the image due the point spread function of the instrument.